

Article

Electron Regulation in Pt-M (M = Cu, Co, and Ni) Decorated WO₃ Thin Films for Photocatalytic Degradation Performance

Jinkang Pan ^{1,2}, Lihua Zhang ^{2,3}, Cunxia Wang ^{2,3}, Kangjie Gao ^{2,3} and Pengyu Dong ^{2,*} 

¹ School of Chemistry and Chemical Engineering, Yancheng Institute of Technology, Yancheng 224051, China; apanjinkang@163.com

² Key Laboratory for Advanced Technology in Environmental Protection of Jiangsu Province, Key Laboratory for Ecological-Environment Materials of Jiangsu Province, Yancheng Institute of Technology, Yancheng 224051, China; zlh1670@163.com (L.Z.); wcx1538975755@163.com (C.W.); gkangjie0922@163.com (K.G.)

³ School of Mechanical Engineering, Yancheng Institute of Technology, Yancheng 224051, China

* Correspondence: dongpy11@gmail.com or dongpy11@ycit.edu.cn

Abstract: In this study, Pt-M/WO₃ (M = Cu, Co, and Ni) thin films are effectively synthesized by preparing homogeneous precursor sols, spin-coating, toluene-etching, and calcination. Furthermore, the microstructural, chemical, and electrochemical properties of the WO₃, Pt-Cu/WO₃, Pt-Co/WO₃, and Pt-Ni/WO₃ thin films are also systematically compared. The results demonstrate that when compared to the WO₃ thin film, the photocatalytic capability for methylene blue (MB) solution degradation is greatly increased in the Pt-M/WO₃ thin films. Transfer routes for photogenerated charges and an improved photocatalytic process are suggested based on the experimental results. Due to the large difference in the work function (Φ) between the bimetallic alloy Pt-M and WO₃, a bending of the energy bands at the Pt-M/WO₃ interface is presented. Furthermore, the introduction of transition metals such as Cu, Co, or Ni modifies the electronic structure of Pt-M/WO₃ thin films, facilitating the separation and migration of electrons and holes. Specifically, the photogenerated electrons migrate from the CB of WO₃ to Pt-Co or Pt-Ni nanoparticles in the samples of Pt-Co/WO₃ or Pt-Ni/WO₃ thin films, while the hot electrons from the localized surface plasmon resonance (LSPR) effect of Cu could transfer to the conduction band (CB) of WO₃ and other electrons generated from the photoexcitation of the WO₃ semiconductor itself in the sample of the Pt-Cu/WO₃ thin film. In summary, this work proposes a unique strategy for creating electron regulation in Pt-M decorated WO₃ thin films for photocatalytic application.

Keywords: photocatalytic degradation; WO₃ thin films; Pt-based bimetallic cocatalysts; electron regulation



Citation: Pan, J.; Zhang, L.; Wang, C.; Gao, K.; Dong, P. Electron Regulation in Pt-M (M = Cu, Co, and Ni) Decorated WO₃ Thin Films for Photocatalytic Degradation Performance. *Catalysts* **2023**, *13*, 1044. <https://doi.org/10.3390/catal13071044>

Academic Editor: Weilin Dai

Received: 11 May 2023

Revised: 3 June 2023

Accepted: 25 June 2023

Published: 28 June 2023



Copyright: © 2023 by the authors. Licensee MDPI, Basel, Switzerland. This article is an open access article distributed under the terms and conditions of the Creative Commons Attribution (CC BY) license (<https://creativecommons.org/licenses/by/4.0/>).

1. Introduction

For the possibility of using them to degrade organic contaminants, semiconductor-based photocatalysts have been the subject of intense study during the last several years [1–3]. With an energy bandgap (E_g) of around 3.2 eV, titanium dioxide (TiO₂) is a well-known conventional semiconducting photocatalyst [4]. Nevertheless, because of its large bandgap, it hardly responds even weakly to ultraviolet light, which only makes up about 4% of sunlight's total energy. Furthermore, the easy recombination of electron–hole pairs produced by light reduces the efficiency of photocatalysis.

As one of the n-type semiconductors and functional materials, tungsten trioxide (WO₃) has been extensively investigated in recent decades and has a wide range of potential applications [5–7]. Due to its smaller bandgap than the popular TiO₂, which possesses a small bandgap of between 2.4 and 2.8 eV and enables it to absorb more solar energy and produce a larger photocurrent, WO₃ has recently attracted attention [8]. In-depth research has shown that the strongly negative charges on the surfaces of WO₃ make them

perfect for use in adsorption applications, especially for cationic dyes such as methylene blue (MB) [9]. Due to its low conduction band (CB) level, WO_3 has a low reduction potential of its electrons, resulting in a lower light energy conversion efficacy than TiO_2 [10]. Researchers have suggested a number of methods for boosting the photocatalytic properties of WO_3 , including supplementation with other elements [11], surface modification with metal nanoparticles [12,13], and the creation of hybrid composites with other materials, to bypass this restriction [14,15]. These techniques may boost the stability, photocatalytic activity, and light absorption characteristics of WO_3 , as well as its photocatalytic efficiency.

Recently, it has been shown that coating WO_3 semiconductors with noble metals is a successful way to increase their photocatalytic activity. Under UV-light irradiation, WO_3 loaded with Pt nanoparticles displayed photocatalytic activity nearly on par with TiO_2 [16,17]. When compared to Pt monometallic cocatalysts, in a lack of light irradiation, Pt-based bimetallic cocatalysts demonstrated a distinct collaborative impact and substantially enhanced their catalytic efficiency. For instance, our group has demonstrated that the Pt-Ag/ WO_3 thin film has a substantially improved photocatalytic performance for MB solution degradation [18]. There has also been research on other Pt-based bimetallic cocatalysts, including Pt-Au [19], Pt-Ru [20], and Pt-Pd [21,22]. Non-precious metals, on the other hand, are being thought of as the second metal to be alloyed with platinum owing to the high price of precious metals. Notably, alloys of metals such as Cu, Co, and Ni with Pt have shown a clear synergistic effect. The interaction between the *d* electron orbitals of these transition metals and Pt leads to electron redistribution, enabling precise control over the electronic structure of Pt. The tunability allows for the modulation of photocatalytic properties and reaction activity, ultimately enhancing the efficiency of photocatalytic reactions. Furthermore, the incorporation of Cu, Co, or Ni within the nanoparticle architecture allows for better utilization of Pt atoms by minimizing the core Pt wastage. This strategy enables a significant reduction in Pt loading without compromising the photocatalytic degradation performance, thus offering a promising avenue for cost reduction. These alloys also have the advantages of being easily accessible and environmentally safe, which reduces the cost of the bimetallic electrocatalysts even more [23–26]. However, there is little research on the bimetallic Pt-M (M represents a non-precious metal element) cocatalyst-decorated WO_3 thin film for photocatalytic degradation.

In this work, the Pt-M/ WO_3 (M = Cu, Co, and Ni) thin films were created by dip-coating deposition of sol-gel precursors onto WO_3 as the support material and incorporating Cu, Co, and Ni into the Pt alloy. The electrical alteration of the surface Pt atoms and the uniform distribution of the resulting bimetallic cocatalysts led to considerable synergistic effects and increased catalytic activity. The presence of Pt could facilitate the migration of photoexcited electrons, and the introduction of these transition metals could result in modifications of the electronic structure, band alignment, and surface properties of the Pt-M/ WO_3 composite. This might lead to improved charge separation, increased visible-light absorption, and enhanced redox reactions, all contributing to the efficient photocatalytic degradation of MB. We suggest paths for photogenerated charge transfer and photocatalytic processes by a methodical comparative examination of the microstructural, chemical, and photoelectrochemical properties of the WO_3 , Pt-Cu/ WO_3 , Pt-Co/ WO_3 , and Pt-Ni/ WO_3 thin films.

2. Results and Discussion

2.1. XRD and Raman Analysis

X-ray diffraction (XRD) patterns were used to identify the crystal phases of the indium tin oxide (ITO) glass and the thin films of WO_3 , Pt-Cu/ WO_3 , Pt-Co/ WO_3 , and Pt-Ni/ WO_3 while they were being manufactured, as shown in Figure 1a. Except for the ITO glass peaks, the results clearly showed that all of the thin films exhibited polycrystalline structures with peaks that corresponded to the cubic phase of WO_3 (JCPDS 41-0905). Due to the relatively thin film thickness, it was found that the ITO glass peak was detected in all the as-prepared thin films. Additionally, no Pt-Cu, Pt-Co, and Pt-Ni diffraction peaks were seen in the

Pt-Cu/WO₃, Pt-Co/WO₃, and Pt-Ni/WO₃ thin films, respectively, suggesting that the composite thin films contained relatively little Pt-M (M = Cu, Co, and Ni).

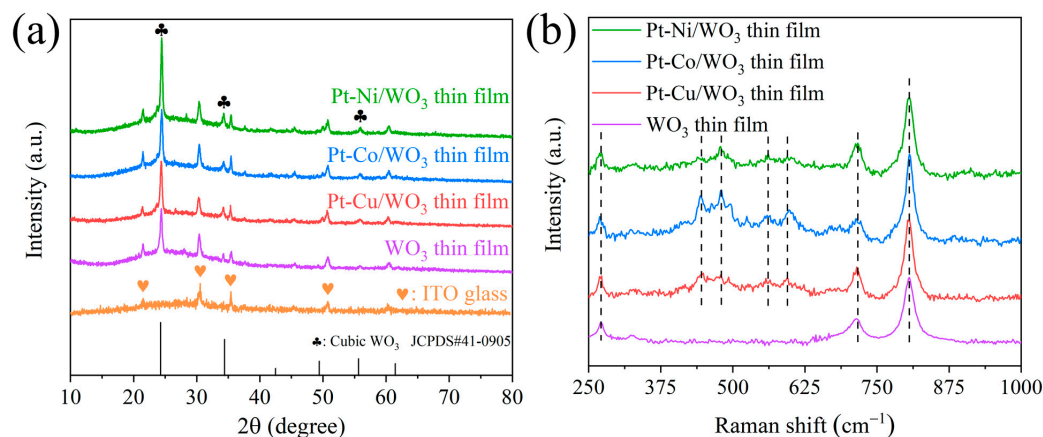


Figure 1. (a) XRD patterns (the orange symbols correspond to the diffraction peaks of ITO glass) and (b) Raman spectra of the WO₃, Pt-Cu/WO₃, Pt-Co/WO₃, and Pt-Ni/WO₃ thin films.

Figure 1b displays the Raman spectra for all the as-prepared thin films. The peak at 269 cm⁻¹ was attributed to the W–O stretching vibrations of the monoclinic WO₃ phase. The major Raman modes seen in all thin films were found at 714 and 806 cm⁻¹, which corresponded to the W–O stretching vibrations [27,28]. In the low wavenumber range, the Raman bands at 445 and 478 cm⁻¹ were ascribed to PtO [29] and Pt–CO stretching with on-top configurations [30], respectively. The overlapping band of the stretching vibrations of Pt–OH and Pt–O ($\nu_{\text{Pt-O(H)}}$) was thus allocated to the bands at 560 and 597 cm⁻¹, respectively [31,32]. These findings support the XRD findings that the obtained bimetallic Pt-M/WO₃ thin films have nearly identical Raman bands.

2.2. XPS Analysis

X-ray photoelectron spectroscopy (XPS) analysis was employed to investigate the chemical binding energies of the WO₃, Pt-Cu/WO₃, Pt-Co/WO₃, and Pt-Ni/WO₃ thin films. The full spectra for all as-prepared thin films revealed the presence of C, O, W, Pt, Cu, Co, and Ni elements, as shown in Figure 2a. The W 4f spectra in Figure 2b showed double peaks at approximately 35.1 and 37.3 eV for WO₃ thin films, which were attributed to W 4f_{7/2} and W 4f_{5/2}, respectively [33]. In comparison with the WO₃ thin film, the binding energies of the W 4f_{7/2} and W 4f_{5/2} peaks for Pt-Cu/WO₃, Pt-Co/WO₃, and Pt-Ni/WO₃ thin films increased by approximately 0.4 eV, indicating a chemical interaction between Pt-M (M = Cu, Co, and Ni) and WO₃ in the thin films, respectively. In accordance with the Raman findings, the XPS analysis of Pt 4f for the Pt-M/WO₃ (M = Cu, Co, and Ni) thin films (Figure 2c) showed two splitting peaks that were assigned to the Pt (II) chemical state (PtO and Pt(OH)₂) in all as-prepared thin films [34,35]. When compared to the typical Pt 4f peak, the binding energies of the Pt-Cu, Pt-Co, and Pt-Ni peaks increased [36,37]. In Figure 2d, the Cu 2p_{3/2} and Cu 2p_{1/2} binding energies of Pt-Cu/WO₃ were determined to be at 932.0 and 952.0 eV, respectively [38,39]. Cu (0) was identified by the greater peak at a lower binding energy of 932.0 eV, whereas Cu (II) and (I) were identified by the weaker peaks at higher binding energies of 934.0 eV and 952.0 eV, respectively [40,41]. Additionally, strong shake-up satellite features at 942.0 eV for Cu 2p_{3/2} and 955 eV for Cu 2p_{1/2} were observed as a fingerprint of the Cu²⁺ species [42]. The peaks of the Co 2p XPS spectrum in Figure 2e were attributed to Co 2p_{1/2} and Co 2p_{3/2}, which represent the species of Co₂O₃ and CoOOH, respectively [43,44]. In Figure 2f, the high-resolution Ni 2p XPS spectrum shows fitting peaks at 878.0 and 859.1 eV, which belonged to Ni 2p_{1/2} and Ni 2p_{3/2}, respectively, and they were ascribed to NiO and Ni(OH)₂ [45,46]. Consequently, these findings support the XPS analysis' finding that the Pt-Cu (Ni, Co) alloy contains oxide species.

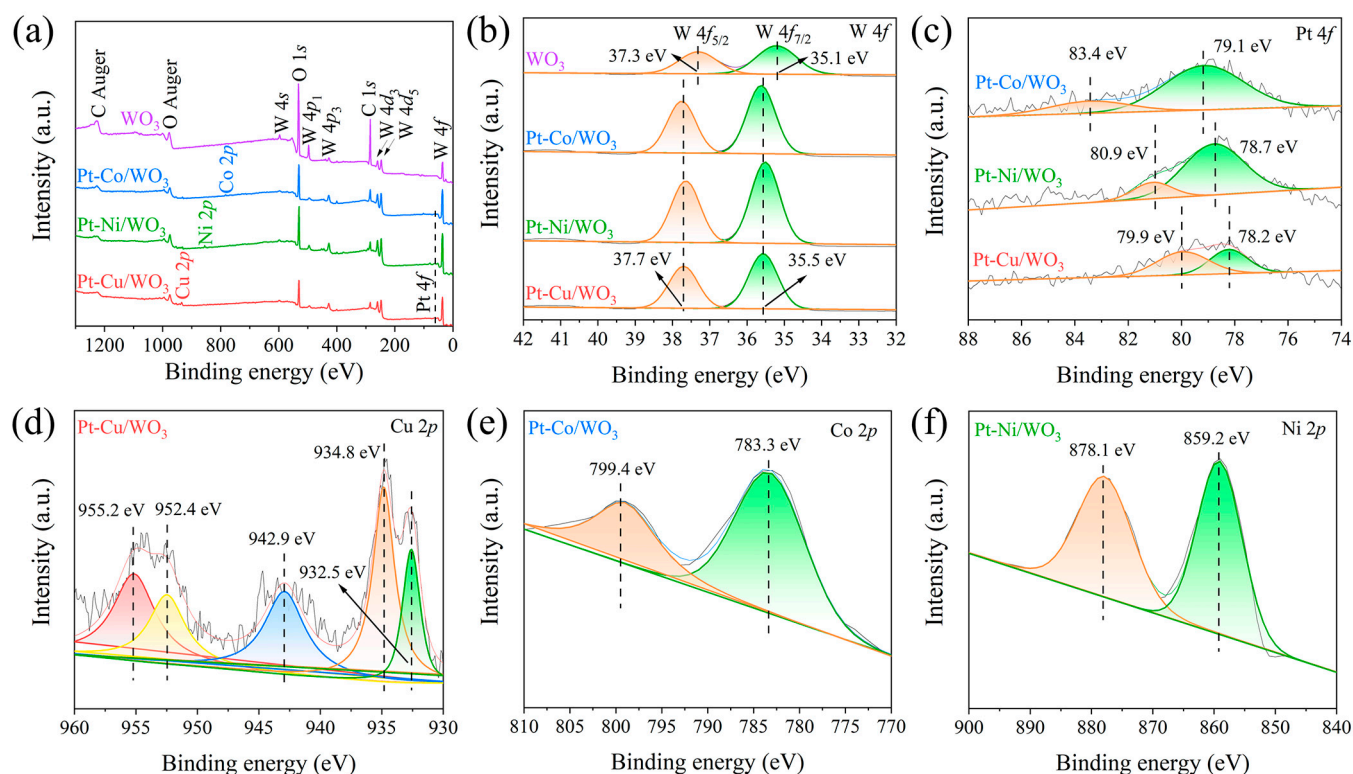


Figure 2. Full XPS spectra (a), high-resolution W 4f (b), Pt 4f (c), Cu 2p (d), Co 2p (e), and Ni 2p (f) XPS spectra of the WO_3 , Pt-Cu/ WO_3 , Pt-Co/ WO_3 , and Pt-Ni/ WO_3 thin films.

2.3. Morphological Features

For the purpose of assessing the surface morphological properties of the thin films in their as-prepared state, scanning electron microscopy (SEM) was used. Figure 3a–d reveals that the WO_3 thin film consisted of compact spherical particles with a size of approximately 50 nm [47]. On the other hand, we demonstrated that the Pt-Cu/ WO_3 , Pt-Co/ WO_3 , and Pt-Ni/ WO_3 thin films exhibited uniform and compact blackberry-like morphologies with little roughness. Moreover, SEM images of the cross-section of the films are provided in Figure 3. It was observed that the thickness of the pure WO_3 , Pt-Cu/ WO_3 , Pt-Co/ WO_3 , and Pt-Ni/ WO_3 thin films was about 66, 68, 75, and 72 μm , respectively. In addition, the corresponding transmission electron microscopy (TEM) and high-resolution TEM (HRTEM) images of the Pt-Cu/ WO_3 thin film are presented in Figure S1 in the Supplementary Material. The HRTEM image revealed distinct lattice fringes corresponding to d-spacing values of 0.371 nm and 0.220 nm (Figure S1c), which can be attributed to the (100) plane of WO_3 and the (111) plane of the Pt-Cu alloy, respectively [34].

2.4. Optical Absorption Characteristics

Figure 4a shows the optical absorption characteristics of the different photocatalysts, as evaluated by UV-vis diffuse reflectance absorption (DRS) spectra. The inter-band optical transition of the WO_3 thin film is responsible for the prominent peaks seen in all thin films below 400 nm [48]. The Pt-Cu/ WO_3 , Pt-Co/ WO_3 , and Pt-Ni/ WO_3 thin films showed an increased absorbance in the visible-light range, which could be owing to the Pt-M particulates scattering light [49,50]. The Pt-Cu/ WO_3 thin film had a significantly widened and intense peak in the 430–550 nm range, suggesting that localized surface plasmon resonance (LSPR) may be responsible for the photothermal effect being shown by the Pt-Cu nanoparticles [38]. Notably, the Cu particles' plasmon resonance absorbance was not obvious, owing to the reduced Cu content of the Pt-Cu/ WO_3 thin film. Furthermore, the WO_3 , Pt-Co/ WO_3 , and Pt-Ni/ WO_3 thin films exhibited comparable absorption spectra to the Pt-Cu/ WO_3 thin film, likely owing to the weakly expressed texture and microcrystalline

structure of the ITO films [51,52]. The following equation was used to obtain the E_g of all the thin films using the value regarding absorption:

$$\alpha hv = A(hv - E_g)^n \quad (1)$$

The absorption coefficient (α), absorption constant (A), and constant (n) are interdependent and vary with the type of electronic transition involved. For direct transitions, the value of n is $1/2$, whereas for indirect transitions, n is 2. The intersection with the tangent in the plots of $(\alpha hv)^{1/2}$ against the energy of photons, hv , was used to determine the E_g values of the thin films since WO_3 showed an indirect bandgap (Figure 4b). According to our research, the WO_3 , Pt-Cu/ WO_3 , Pt-Co/ WO_3 , and Pt-Ni/ WO_3 thin films had E_g values of 2.63, 2.54, 2.60, and 2.57 eV, respectively. Future research is required to ascertain whether alterations in the electronic structure of the WO_3 film result in a reduction in the bandgap energy of the Pt-Cu/ WO_3 , Pt-Co/ WO_3 , and Pt-Ni/ WO_3 thin films relative to the WO_3 film.

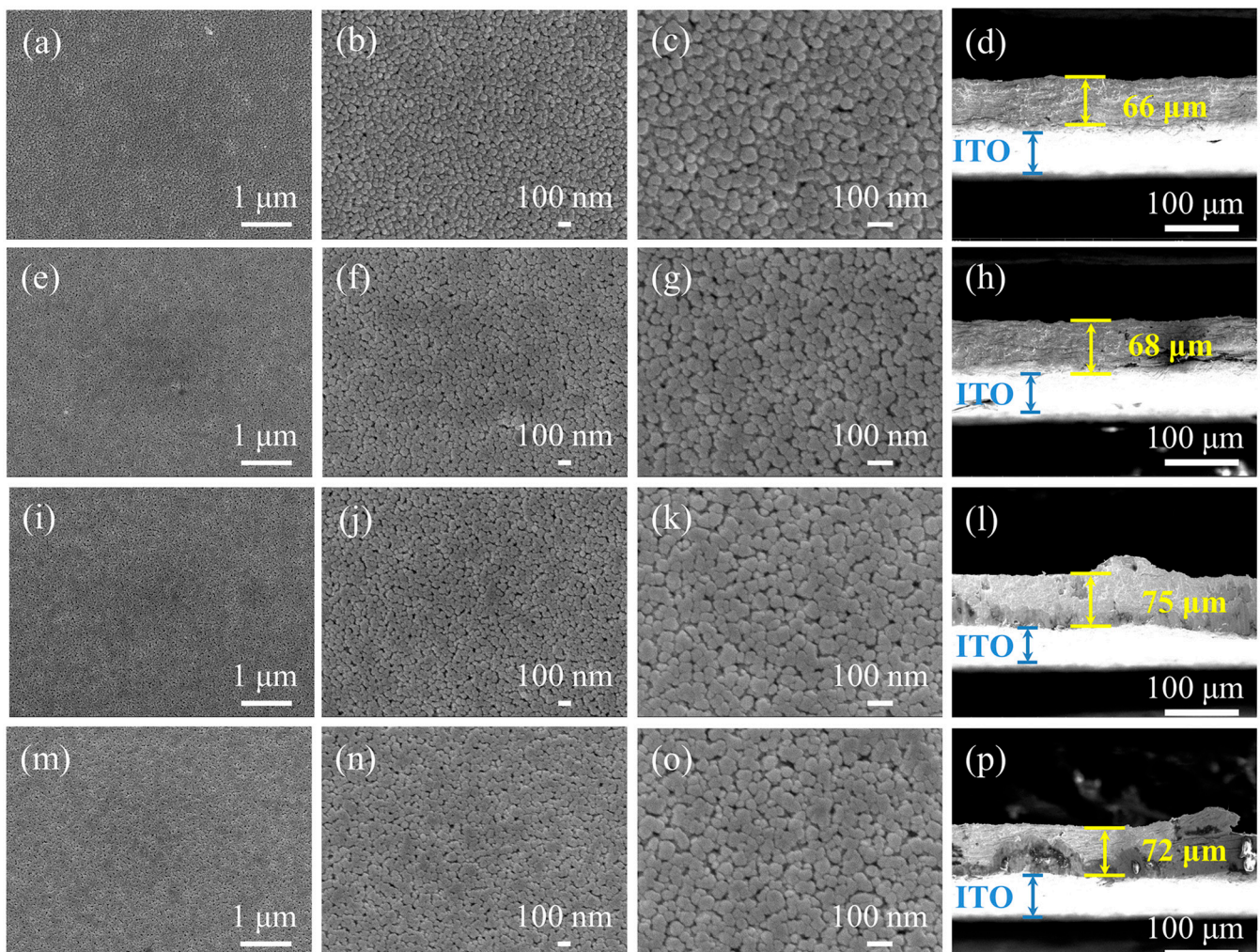


Figure 3. SEM images of (a–d) WO_3 , (e–h) Pt-Cu/ WO_3 , (i–l) Pt-Co/ WO_3 , and (m–p) Pt-Ni/ WO_3 thin films.

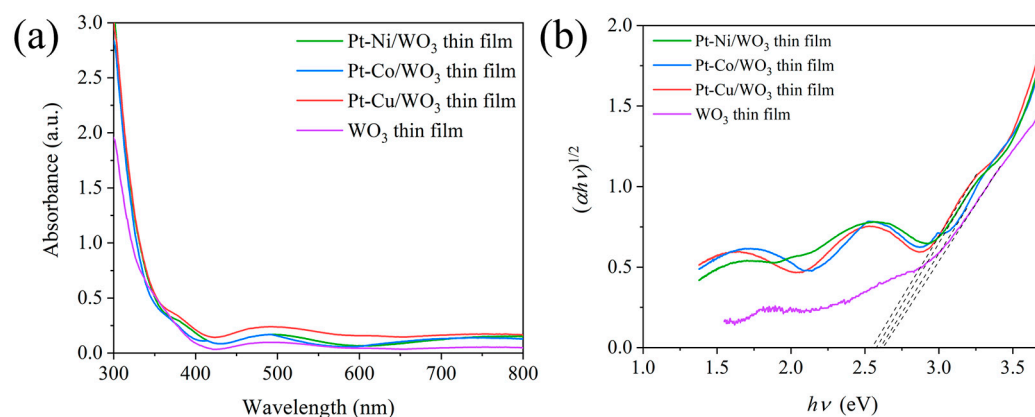


Figure 4. (a) UV-vis DRS spectra of the WO_3 , Pt-Cu/ WO_3 , Pt-Co/ WO_3 , and Pt-Ni/ WO_3 thin films (the inset shows the region from 400 to 800 nm). (b) Plots of $(\alpha h\nu)^{1/2}$ versus photon energy $h\nu$ of these thin films.

2.5. Photocatalytic Degradation Performance

The adsorption isotherms before the irradiation process of Pt-M/ WO_3 were measured and provided in Figure S2. It was observed that adsorption–desorption equilibrium was achieved within 40 min in the darkness. Due to its low self-degradation under visible light, the pollutant MB was selected to test the photocatalytic efficiency of the synthesized thin films. The efficiency of the photocatalytic degradation of the MB solution measured and plotted in the presence of WO_3 , Pt-Cu/ WO_3 , Pt-Co/ WO_3 , and Pt-Ni/ WO_3 thin films is shown in Figure 5a. With a degradation efficiency of 98.9% after 120 min, the Pt-Cu/ WO_3 thin film exhibited the greatest photocatalytic efficiency of all the thin films tested, whereas the WO_3 thin film only managed a 60% degradation efficiency under the same circumstances. Such a high photocatalytic efficiency value for the Pt-Cu/ WO_3 thin film exceeded most of the previously reported WO_3 -based photocatalysts (Table S1). The Pt-Co/ WO_3 and Pt-Ni/ WO_3 thin films also exhibited good photocatalytic activity, with degradation efficiencies of approximately 88% and 90%, respectively. Despite the low initial concentration of MB (5 mg L^{-1}), it is crucial to remember that the total degradation of MB under the condition of the Pt-Cu/ WO_3 thin film required a lengthy irradiation time of nearly 120 min. This was primarily produced by placing the thin film photocatalyst on a substrate, which resulted in reduced light absorption and pollutant–molecule interactions. As a result, thin-film photocatalysts usually have lower photocatalytic activity than powder photocatalysts. While conventional powder photocatalysts could undergo laborious recycling procedures, thin-film photocatalysts have the advantages of easy reuse and minimal loss during photocatalytic reactions.

By employing the Langmuir–Hinshelwood model, it was found that the degradation of dyestuffs occurred through a pseudo-first-order reaction, as long as the initial concentration (C_0) of the dyestuff solution was low. This model assumes that the photocatalytic degradation proceeds via a rapid surface adsorption and reaction step, with the reaction rate being proportional to the concentration of MB. The concentration of the Pt-M/ WO_3 catalyst had a minor influence on the reaction rate in this model [53–55]:

$$\ln(C_0/C) = kt \quad (2)$$

where C , C_0 , k , and t are the remaining concentration of MB solution, the initial concentration, the rate constant of a first-order reaction, and the irradiation time, respectively. Among them, the Langmuir–Hinshelwood model was utilized in the pseudo-first-order reaction kinetics with a 5 mg L^{-1} initial concentration of MB in our study. The graph of $\ln(C_0/C)$ vs. irradiation time is presented in Figure 5b, and a steeper slope implies a quicker rate of MB solution degradation. Using the Langmuir–Hinshelwood model, the rate constant of a first-order reaction was estimated. The rate constant of a first-order reaction in the

Pt-Cu/WO₃ thin film was discovered to be approximately 6 times larger compared to that found in the WO₃ thin film. Furthermore, the correlation coefficient (R^2) was used to evaluate the relationship between the actual practical photocatalytic reaction data and the linear fitting model [56]. It was observed that all the fabricated thin films exhibited R^2 values exceeding 0.9, suggesting that the experimental results conformed to the first-order kinetics.

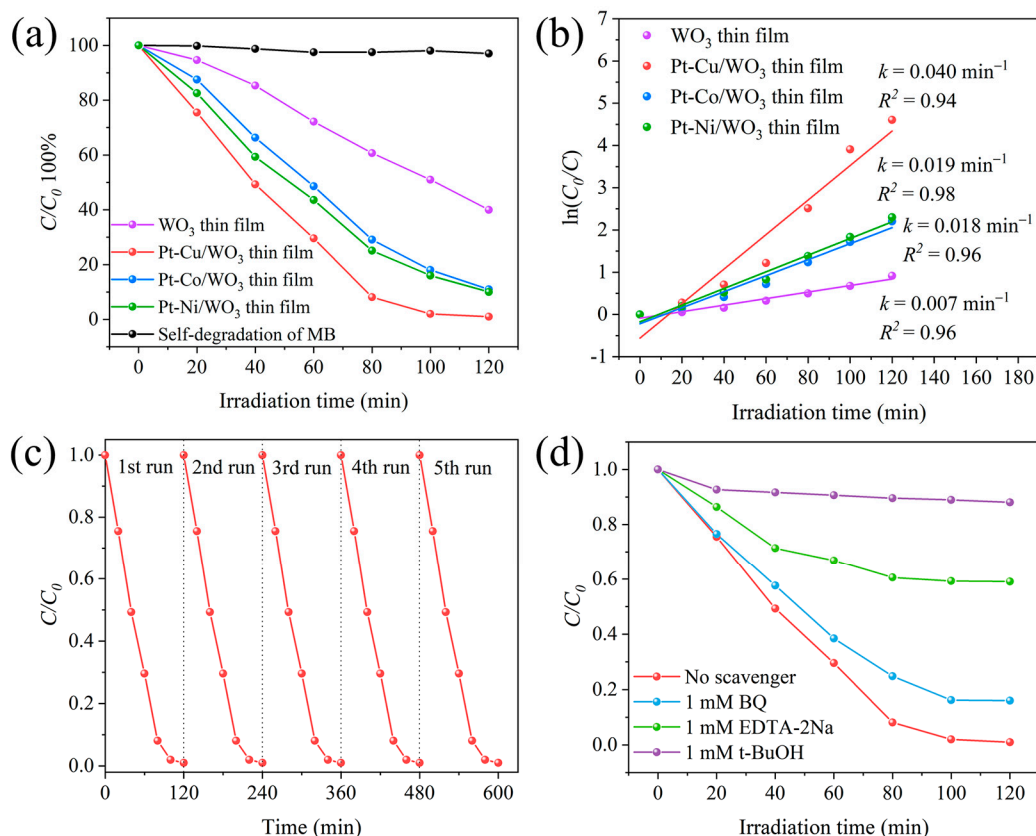


Figure 5. (a) Photocatalytic degradation ratio of MB solution in the presence of WO₃, Pt-Cu/WO₃, Pt-Co/WO₃, and Pt-Ni/WO₃ thin films. (b) Plots of $\ln(C_0/C)$ versus irradiation time. (c) Recycling experiments towards MB degradation over the Pt-Cu/WO₃ thin film. (d) Plots of photogenerated carrier-trapping during the photodegradation of MB by the Pt-Cu/WO₃ thin film under visible-light irradiation.

MB was degraded in numerous cycling cycles in order to evaluate the recycling photostability of the Pt-Cu/WO₃ thin-film catalyst, as shown in Figure 5c. The results showed that even after five cycles, the Pt-Cu/WO₃ thin film still maintained an excellent degradation rate under light irradiation. The photocatalytic stability of the Pt-Cu/WO₃ thin film for MB degradation was remarkable, according to our unmistakable data.

It is crucial to carry out free radical and hole-trapping studies to identify these species in order to assure the formation of active species during the photodegradation process in photocatalytic reactions. In our study, we utilized ethylene diamine tetraacetic acid disodium salt (EDTA-2Na), 1,4-benzoquinone (BQ), and *tert*-butyl alcohol (*t*-BuOH) as scavengers to trap the superoxide anion radical ($\bullet\text{O}_2^-$), the hole (h^+), and the hydroxy radical ($\bullet\text{OH}$), respectively [57–59]. Figure 5d illustrates how the various scavengers affected the photocatalytic activity of the Pt-Cu/WO₃ thin film for MB photodegradation under visible light. The reaction system with the addition of BQ (1 mM) did not noticeably inhibit the photodegradation efficiency of MB, compared to the Pt-Cu/WO₃ thin-film system without any scavenger. However, the photodegradation efficiency of MB was clearly decreased after adding EDTA-2Na (1 mM) to the system. Additionally, the photocatalytic

degradation activity of the Pt-Cu/WO₃ thin film also showed a significant decrease after adding *t*-BuOH (1 mM) to the system. These research results indicate that under visible-light exposure, •OH was the primary active species that facilitated the oxidization of MB, while h⁺ was also one of the reactive species. Furthermore, in the Pt-Cu/WO₃ thin-film photocatalytic degradation system, •O₂[−] was produced in negligible amounts.

2.6. Photogenerated Chargers Separation and Migration

The photoelectrochemical (PEC) characteristics of the several as-prepared thin films were assessed under AM 1.5 G exposure at 100 mW cm^{−2} in the 0.5 M Na₂SO₄ solution. The linear sweep voltammetry (LSV) curves of the as-prepared thin films are shown in Figure 6a. The photocurrent density of the WO₃ thin film was 0.65 mA cm^{−2} at 1.23 V vs. RHE. In contrast, the photocurrent density of Pt-Cu/WO₃, Pt-Co/WO₃, and Pt-Ni/WO₃ thin films was ca. 5.81 mA cm^{−2}, 5.01 mA cm^{−2}, and 4.74 mA cm^{−2}, respectively, at 1.23 V vs. RHE, which were almost 8.9, 7.7, and 7.3 times higher than that of the WO₃ thin film. These findings imply that the Pt-Cu/WO₃, Pt-Co/WO₃, and Pt-Ni/WO₃ thin films could effectively reduce electron–hole recombination in the PEC reaction and increase effective electron mobility, resulting in improved photocatalytic properties. Furthermore, the slopes of the curves for Pt-Cu/WO₃, Pt-Co/WO₃, and Pt-Ni/WO₃ thin films in the 0.9 to 1.2 V vs. RHE region were significantly steeper than that of the bare WO₃ thin film, indicating that these thin films had higher carrier-filling factors.

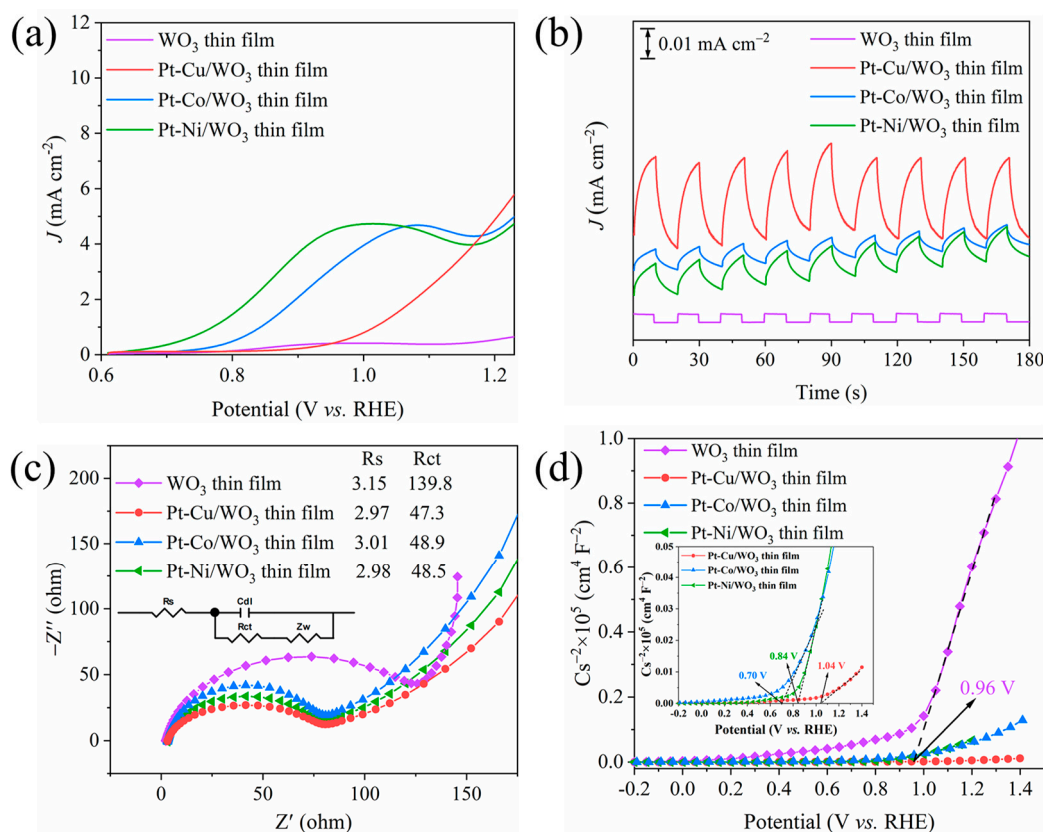


Figure 6. (a) Comparison of LSV curves of WO₃, Pt-Cu/WO₃, Pt-Co/WO₃, and Pt-Ni/WO₃ thin films. (b) Transient photocurrent responses in several on–off cycles. (c) Nyquist plots of EIS of as-prepared thin films with AM 1.5 G and bias of 1.23 V vs. RHE. (d) Mott–Schottky plots of all thin films measured in the dark at 1 kHz (the inset is the enlarged part for the three thin films).

The transient photocurrent responses of the different thin films were examined under chopped AM 1.5 G exposure with a bias of 0.2 V in order to examine the effectiveness of charge separation, as shown in Figure 6b. The transient photocurrent density describes

the sequence of Pt-Cu/WO₃, Pt-Ni/WO₃, Pt-Co/WO₃, and WO₃ among the as-prepared thin films. The Pt-Cu/WO₃ thin film had the strongest photocurrent response in numerous on–off cycles, which was notable. Additionally, when the light source was turned on and off, distinct transient anodic peaks could be seen in the Pt-Cu/WO₃, Pt-Co/WO₃, and Pt-Ni/WO₃ thin films. This suggests that photogenerated holes from the WO₃ thin film may be stored in the Pt-Cu, Pt-Co, and Pt-Ni layers, preventing the recombination of photogenerated electron–hole pairs. This result suggests that the Pt-Cu, Pt-Co, and Pt-Ni layers could act as efficient hole storage layers for capturing and accumulating photogenerated holes.

Through electrochemical impedance spectroscopy (EIS), a comparison of the semicircular Nyquist plot diameter was performed, and the resultant Nyquist plots were matched to assess the electron transfer resistance (R_{ct}) with an analogous circuit using Zview software [60]. The fitting results showed that the R_{ct} values of Pt-Cu/WO₃ (47.3 Ω), Pt-Co/WO₃ (48.9 Ω), and Pt-Ni/WO₃ (48.5 Ω) were considerably lower than that of WO₃ (139.8 Ω), as presented in Figure 6c. The incorporation of Pt-Cu, Pt-Co, and Pt-Ni alloy nanoparticles significantly improved the charge transfer because they were more efficient at capturing electrons from the CB of WO₃, as shown by the fact that the Pt-Cu/WO₃, Pt-Co/WO₃, and Pt-Ni/WO₃ thin films exhibited a smaller semicircle than the WO₃ thin-film electrodes.

To determine the semiconductor type and the flat-band potentials (E_{fb}), Mott–Schottky plots were employed, and the findings are depicted in Figure 6d. The calculated E_{fb} values of WO₃, Pt-Cu/WO₃, Pt-Co/WO₃, and Pt-Ni/WO₃ thin films were 0.96, 1.04, 0.70, and 0.84 V vs. RHE, respectively, and were similar to each other. The positive slopes of all four curves implied that the thin films were composed of n-type semiconductors. It should be noted that the slope of the Pt-Cu/WO₃ thin-film curve was lower than that of the WO₃, Pt-Co/WO₃, and Pt-Ni/WO₃ thin-film curves, which implies that the concentration of carriers in the former was higher and the transfer rate of photogenerated electrons was faster. This is important to note because there is an inverse correlation between the slopes and the charge carrier density [61]. These results showed that charge transfer was better-facilitated by Pt-Cu/WO₃, Pt-Co/WO₃, and Pt-Ni/WO₃ thin films than by WO₃, and that the photocatalytic activity was significantly increased.

Based on the information that is currently accessible, the energy-level diagram of WO₃, Pt-Cu/WO₃, Pt-Co/WO₃, and Pt-Ni/WO₃ thin films was provided. Figure 7 illustrates the energy-level diagram obtained from the Mott–Schottky plot, where the positive slope (Figure 6d) suggests that the material exhibited n-type semiconductor properties, and the conduction band minimum (E_{CBM}) was approximately equal to the E_{fb} . Additionally, the bandgaps were determined as 2.63, 2.54, 2.60, and 2.57 eV, respectively, by extrapolating the intercept on the x -axis in the linear region of the Tauc plot (Figure 4b). Consequently, the valence band positions (E_{VB}) of WO₃, Pt-Cu/WO₃, Pt-Co/WO₃, and Pt-Ni/WO₃ thin films were inferred to be 3.59, 3.58, 3.30, and 3.41 V, respectively.

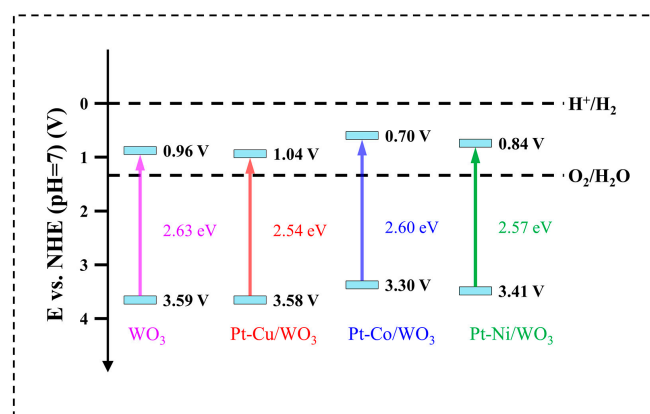
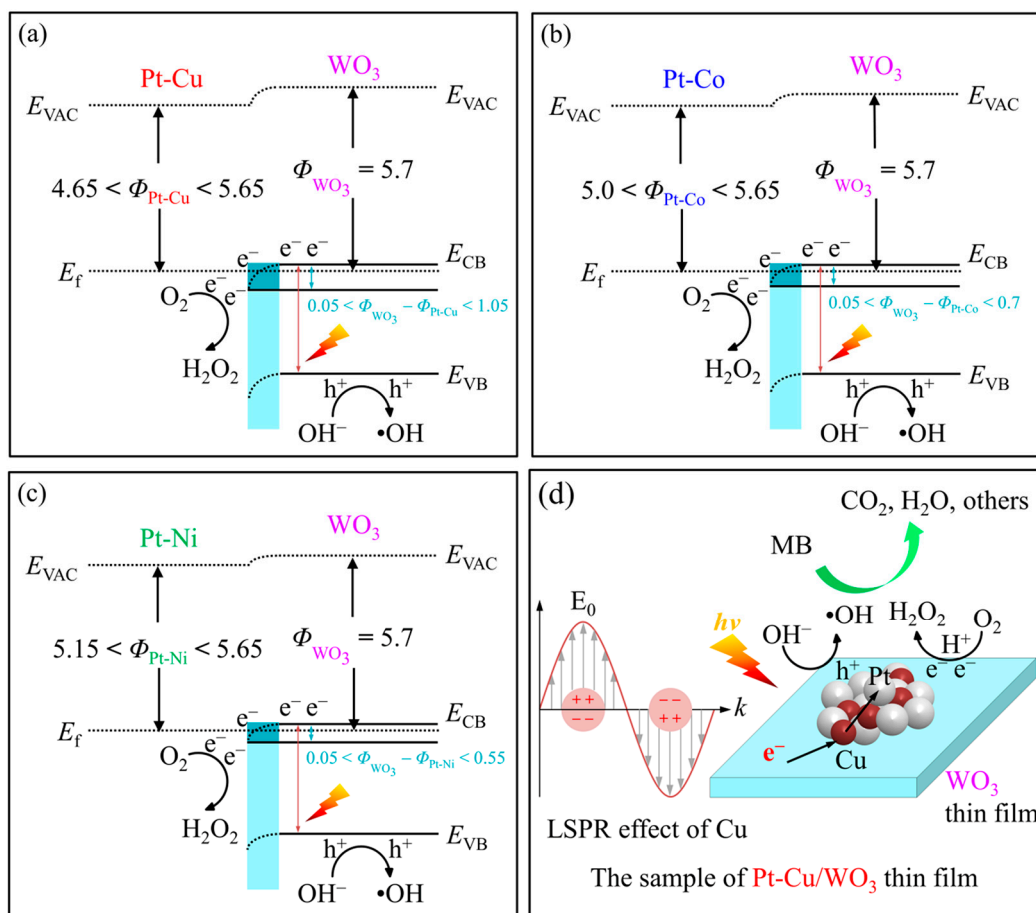


Figure 7. Schematic energy-level diagram of WO₃, Pt-Cu/WO₃, Pt-Co/WO₃, and Pt-Ni/WO₃ thin films.

2.7. Photocatalytic Mechanism Analysis

Understanding the increased photocatalytic activity requires research into the improved photocatalytic mechanism. We have presented a thorough description based on the band structure and work functions in this study. The work functions (Φ) of the WO_3 thin film, metallic Pt, metallic Cu, metallic Co, and metallic Ni were reported to be 5.7 eV, 5.65 eV, 4.65 eV, 5.0 eV, and 5.15 eV, respectively [62–65]. Moreover, the work function of the bimetallic alloy Pt-M (M = Cu, Co, and Ni) can be calculated as the sum of the work functions of the two metals [66], indicating that the work function of the alloy is at an intermediate level between two monometallic Pt and Cu (Co or Ni) ($4.65 \text{ eV} < \Phi_{\text{Pt-Cu}} < 5.65 \text{ eV}$, $5.0 \text{ eV} < \Phi_{\text{Pt-Co}} < 5.65 \text{ eV}$, and $5.15 \text{ eV} < \Phi_{\text{Pt-Ni}} < 5.65 \text{ eV}$). When Pt-M (M = Cu, Co, and Ni) came into contact with WO_3 , the charges transferred from Pt-M (M = Cu, Co, and Ni) to the CB of WO_3 to achieve Fermi-level equilibrium. Consequently, the accumulation of excess electrons on the surface area of WO_3 and the excess of positive charge by Pt-M (M = Cu, Co, and Ni) led to a bending of the energy bands at the Pt-M/ WO_3 interface (M = Cu, Co, and Ni). As demonstrated in Scheme 1a–c, the distinction between the WO_3 and bimetallic work functions ($\Phi_{\text{WO}_3} - \Phi_{\text{Pt-M}}$) at the Pt-Cu/ WO_3 , Pt-Co/ WO_3 , or Pt-Ni/ WO_3 juncture was merely approximately 0.05–1.05 eV, 0.05–0.7 eV, and 0.05–0.55 eV, respectively. Under visible-light illumination, when the WO_3 thin-film catalyst was exposed, the photoinduced electrons (e^-) in the valence band (VB) of WO_3 were promoted to the CB, and at the same time, an equal number of photoinduced h^+ were produced in the VB. The introduction of transition metals such as Cu, Co, or Ni modified the electronic structure of Pt-M/ WO_3 thin films, facilitating the separation and migration of electrons and holes. Specifically, the photogenerated electrons migrated from the CB of WO_3 to Pt-Co or Pt-Ni nanoparticles in the samples of Pt-Co/ WO_3 or Pt-Ni/ WO_3 thin films, while the hot electrons from the LSPR effect of Cu could transfer to the CB of WO_3 and other electrons generated from the photoexcitation of the WO_3 semiconductor itself in the sample of Pt-Cu/ WO_3 thin films. Additionally, in the space charge region, the rapidly occurring transport of the photoinduced electrons from WO_3 to Pt-M (M = Cu, Co, and Ni) nanoparticles was rendered achievable by the downward band bending, lowering the recombining of the photoexcited charges and holes. The low CB energy level (1.04 V, 0.70 V, and 0.84 V) of Pt-Cu/ WO_3 , Pt-Co/ WO_3 , and Pt-Ni/ WO_3 thin films was more positive compared to the reduction potential of oxygen for one electron [16], indicating that WO_3 is more capable of accepting electrons. Consequently, the accumulated electrons on Pt-Cu/ WO_3 , Pt-Co/ WO_3 , or Pt-Ni/ WO_3 nanoparticles may transfer to oxygen molecules adsorbed on the surface, forming H_2O_2 through the multi-electron reduction of molecular oxygen [8]. In the Pt-Cu/ WO_3 , Pt-Co/ WO_3 , and Pt-Ni/ WO_3 thin films, an electron donation from Cu (Co and Ni) to Pt may occur since Pt (2.28) exhibited a greater electronegativity compared to Cu (1.93), Co (1.88), and Ni (1.91), causing an electron-rich state in Pt atoms. In other words, the efficient transfer of two electrons for O_2 reduction in the Pt-Cu/ WO_3 , Pt-Co/ WO_3 , and Pt-Ni/ WO_3 thin films is believed to be promoted by the photoexcited electrons from the CB of the WO_3 being transported first to Cu (Co or Ni), and subsequently to Pt, as demonstrated in Scheme 1d. Additionally, this mechanism caused O_2 to undergo a double-electron reduction on the Pt surface rather than on Cu (Co or Ni), thus preventing contact between O_2 and Cu (Co or Ni) and suppressing the oxidation of Cu (Co or Ni) during photodegradation in the presence of the atmosphere. The presence of these alloys increased the yield of H_2O_2 on the Pt-Cu/ WO_3 , Pt-Co/ WO_3 , and Pt-Ni/ WO_3 thin-film catalysts, similar to those observed in Au-Ag/ TiO_2 catalysts [67]. Additionally, surface-bound H_2O or OH^- readily reacted with the departing h^+ to form $\bullet\text{OH}$ due to its strong oxidizing potential (+3 V vs. NHE) [68], in agreement with the results of investigations using photoinduced carrier-trapping (Figure 5d). Furthermore, it has been reported that H_2O_2 can degrade dye molecules [69]. Thus, under the influence of reactive oxidative species such as $\bullet\text{OH}$ and H_2O_2 , thin-film photocatalysts made of Pt-Cu/ WO_3 , Pt-Co/ WO_3 , and Pt-Ni/ WO_3 can efficiently destroy the adsorbed MB molecules during visible-light exposure.



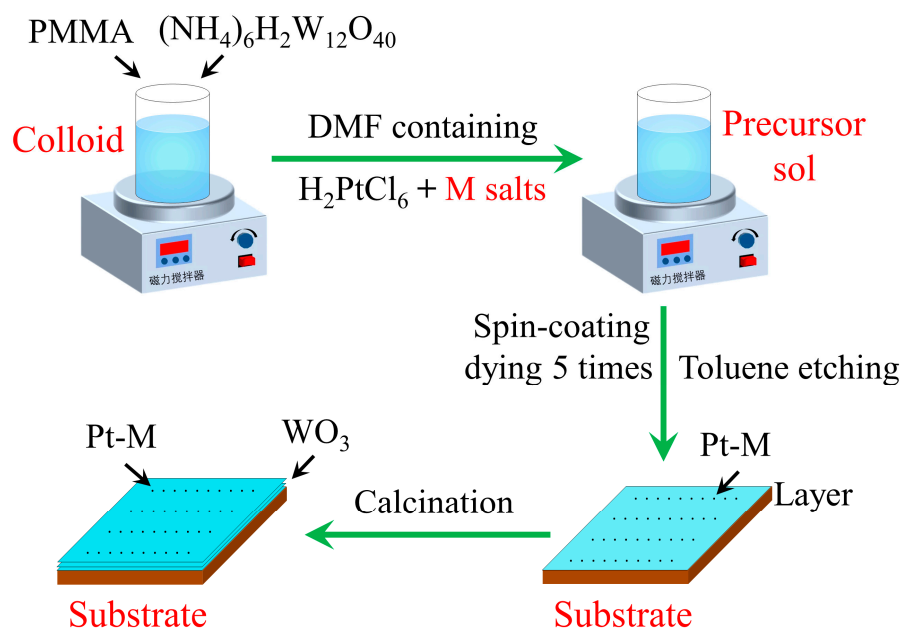
Scheme 1. Schematic energy-band diagrams for (a) Pt-Cu/WO₃, (b) Pt-Co/WO₃, and (c) Pt-Ni/WO₃ thin films (E_{VAC} , E_{CB} , E_{VB} , E_f , Φ_{Pt-M} , and Φ_{WO_3} denote vacuum level, Fermi level, CB level, VB level, the work function of bimetallic cocatalysts, and the work function of WO₃, respectively (in eV)). (d) The photocatalytic mechanism for the degradation of MB on the Pt-Cu/WO₃ thin-film catalyst.

3. Materials and Methods

3.1. Preparation of Pt-M/WO₃ (M = Cu, Co, and Ni) Thin Films

First, the colloidal poly(methyl methacrylate) (PMMA) aqueous suspension, which was previously prepared and described in the Supplementary Material of [70], was used to dissolve 0.3460 g of ammonium paratungstate ((NH₄)₆H₂W₁₂O₄₀) in order to create the WO₃ precursor suspension. The resulting mixture was then stirred at ambient temperatures for a few minutes in order to create a homogeneous suspension. Secondly, the aforementioned precursor solution (2 mL) was then combined with H₂PtCl₆ (0.5 mL 10 mM) and CuCl₂ (or CoCl₂·6H₂O or Ni(NO₃)₂·6H₂O) (0.5 mL 10 mM) in *N,N'*-dimethylformamide (DMF) solution. The combination was then agitated and blended to create a homogeneous suspension. Next, the thin film was then dried in air for around 10 min at 60 °C after 3 mL of the suspension had been spin-coated for 50 s at 3000 rpm onto a 3 × 3 cm ITO substrate. The aforementioned procedure was repeated 5 times, then toluene was used to etch the thin films for 5 min, removing majority of the organic template. Finally, in order to thoroughly break down the PMMA residue, they were then annealed at 450 °C (heating rate 2 °C min⁻¹) in a stream of air (80 cm³ min⁻¹) for 5 h. The procedure for growing is depicted in Scheme 2 as a diagrammatic illustration.

For the sake of comparison, without the addition of H₂PtCl₆ and CuCl₂ (CoCl₂·6H₂O or Ni(NO₃)₂·6H₂O) to the DMF solution, the WO₃ thin film was created under identical circumstances.



Scheme 2. Schematic illustration of the preparation process of the Pt-M/WO₃ (M = Cu, Co, and Ni) thin films.

3.2. Characterization

The D/max-2400 diffractometer (Rigaku, Tokyo, Japan) was used to conduct XRD tests utilizing Cu-K α radiation. Raman spectra were obtained on the Thermo Fischer DXR by using a 532 nm laser as the light source. With the use of SEM (Nova NanoSEM 450, FEI, Hillsboro, OR, USA), the surface morphologies were examined. TEM images were collected with a JEM-2100F electron microscope (JEOL, Tokyo, Japan). In order to explore the surface chemical compositions and states, XPS measurements were performed using Al K α X-ray ($h\nu = 1486.6$ eV) radiation (K-Alpha, Thermo Electron, Waltham, MA, USA). On a UV-vis spectrophotometer (UV-2600, Shimadzu, Kyoto, Japan), diffuse reflectance spectra in the UV-vis range were obtained.

3.3. Photocatalytic Tests

The degradation process of MB in an aqueous solution was used to assess the visible-light photocatalyst according to the procedure for testing photocatalytic materials for the purification of the water solution (GB/T 23762-2009, China). In a standard photocatalytic experiment, the as-prepared thin films employing ITO glass as the support were mounted in a quartz frame and immersed in MB solution (5 mg L⁻¹, 100 mL). To ensure the formation of an equilibrium between adsorption and desorption, the solution was magnetically agitated for 40 min in the dark before irradiation. The visible-light irradiation source, a 350 W Xe lamp with a cutoff filter of 420 nm, was used and placed 10 cm from the reactor. After the light was turned on, 4 mL of a clear MB solution was removed at predetermined intervals (20 min) and analyzed by noting the maximum absorbance of MB at 664 nm in the UV-visible spectrum. C/C_0 was used for determining the proportion of degradation, where C is the concentration of leftover MB solution at each irradiated time interval, and C_0 is the initial concentration.

Utilizing the film in numerous cycles of the photocatalytic degradation of MB allowed the researchers to examine the photocatalytic stability of the ideal Pt-Cu/WO₃ thin film. The photocatalyst was filtered and properly cleaned with deionized water after completing one cycle. The next cycle was then started by adding 5 mg L⁻¹ of fresh MB solution to the photocatalyst. Each cycle took 120 min to complete, and there were 5 cycles in a row.

Experiments were performed to explore the photocatalytic process using active species capture. The MB aqueous solution was supplemented with several radical scavengers,

including *t*-BuOH (1 mmol L⁻¹), EDTA-2Na (1 mmol L⁻¹), and BQ (1 mmol L⁻¹). The subsequent experimental procedures mirrored the photocatalytic test described above.

3.4. PEC Measurements

PEC measurements were conducted using a three-electrode setup and a quartz cell on the electrochemical workstation (CHI660E, Shanghai Chenhua Instruments Co., Ltd., Shanghai, China). As the electrolyte, a 0.5 M Na₂SO₄ solution was utilized. With a surface area of 2.2 cm², the as-obtained thin films were employed as photoanodes. The reference electrode was formed of an Ag/AgCl (saturated KCl) electrode, while the cathode was a Pt sheet. As the lamp housing for the PEC measurement, a simulated sunshine Xe lamp (CEL-HXF300, NbeT Group Corp., Beijing, China) with an AM 1.5 G filter was used. The light power density (i.e., light intensity) was tuned to be 100 mW cm⁻², which was validated by an optical power meter (Model 843-R, Newport, Irvine, CA, USA). On the CHI660E electrochemical workstation, the LSV curves with a scan rate of 10 mV s⁻¹, transient photocurrent responses, EIS, and Mott-Schottky plots were performed.

4. Conclusions

In the present study, homogeneous precursor sols, spin-coating, toluene-etching, and calcination procedures were used to effectively synthesize WO₃, Pt-Cu/WO₃, Pt-Co/WO₃, and Pt-Ni/WO₃ thin films. In conclusion, the resultant thin films had comparable morphologies and were mostly made of low-roughness, blackberry-like particles. The XPS investigation showed a modification in the electrical structure of Pt when alloyed with Cu (Co, Ni). The Pt-Cu/WO₃, Pt-Co/WO₃, and Pt-Ni/WO₃ thin films considerably enhanced the charge transfer and photocatalytic activity compared to the WO₃ thin film, according to the EIS and Mott-Schottky plot analyses. Capture experiments of active species demonstrated that •OH is essential for the oxidization of MB. Furthermore, the introduction of transition metals such as Cu, Co, or Ni modified the electronic structure of Pt-M/WO₃ thin films, facilitating the separation and migration of electrons and holes. Specifically, the photogenerated electrons migrated from the CB of WO₃ to Pt-Co or Pt-Ni nanoparticles in the samples of Pt-Co/WO₃ or Pt-Ni/WO₃ thin films, while the hot electrons from the LSPR effect of Cu could transfer to the CB of WO₃ and other electrons generated from the photoexcitation of the WO₃ semiconductor itself in the sample of Pt-Cu/WO₃ thin films.

Supplementary Materials: The following supporting information can be downloaded at: <https://www.mdpi.com/article/10.3390/catal13071044/s1>. Synthesis of polymethylmethacrylate (PMMA) spheres; Supplementary Figures and Table [71–79]. Figure S1. (a,b) TEM and (c) HRTEM images of Pt-Cu/WO₃ thin film. Figure S2. The adsorption isotherms of MB in the presence of as-prepared samples under dark conditions. Table S1. Comparison between this research and some commonly used WO₃-based photocatalysts for the removal of organic pollutants.

Author Contributions: Conceptualization, P.D.; methodology, J.P.; software, L.Z.; validation, C.W.; formal analysis, K.G.; investigation, J.P.; resources, P.D.; data curation, J.P.; writing—original draft preparation, J.P.; writing—review and editing, P.D.; visualization, J.P.; supervision, P.D.; project administration, P.D.; funding acquisition, P.D. All authors have read and agreed to the published version of the manuscript.

Funding: This work has been funded by the National Natural Science Foundation of China (Grant No. 21403184), the Qinglan Project of Jiangsu Province, the Natural Science Foundation of the Jiangsu Higher Education Institutions of China (Grant No. 22KJA430008), and the Scientific Research and Practical Innovation Project for Graduate Students in Jiangsu Province (No. KYCX22_XY002).

Data Availability Statement: Data are available upon request from the authors.

Conflicts of Interest: The authors declare no conflict of interest.

References

1. Chen, C.; Ma, W.; Zhao, J. Semiconductor-mediated photodegradation of pollutants under visible-light irradiation. *Chem. Soc. Rev.* **2010**, *39*, 4206–4219. [[CrossRef](#)] [[PubMed](#)]
2. Dong, P.; Dong, F.; Fiorenza, R. Photocatalysts for air purification: Design, synthesis, and mechanism investigations. *Front. Chem.* **2022**, *10*, 870550. [[CrossRef](#)] [[PubMed](#)]
3. Suhaimi, N.A.A.; Kong, C.P.; Shahri, N.N.M.; Nur, M.; Hobley, J.; Usman, A. Dynamics of diffusion- and Immobilization-limited photocatalytic degradation of dyes by metal oxide nanoparticles in binary or ternary solutions. *Catalysts* **2022**, *12*, 1254. [[CrossRef](#)]
4. Piątkowska, A.; Janus, M.; Szymański, K.; Mozia, S. C-, N- and S-doped TiO₂ photocatalysts: A review. *Catalysts* **2021**, *11*, 144. [[CrossRef](#)]
5. Dong, P.; Hou, G.; Xi, X.; Shao, R.; Dong, F. WO₃-based photocatalysts: Morphology control, activity enhancement and multifunctional applications. *Environ. Sci. Nano* **2017**, *4*, 539–557. [[CrossRef](#)]
6. Ni, Z.; Wang, Q.; Guo, Y.; Liu, H.; Zhang, Q. Research progress of tungsten oxide-based catalysts in photocatalytic reactions. *Catalysts* **2023**, *13*, 579. [[CrossRef](#)]
7. Wang, Z.; Zhu, C.; Ni, Z.; Hojo, H.; Einaga, H. Enhanced photocatalytic benzene oxidation to phenol over monoclinic WO₃ nanorods under visible light. *ACS Catal.* **2022**, *12*, 14976–14989. [[CrossRef](#)]
8. Sun, S.; Wang, W.; Zeng, S.; Shang, M.; Zhang, L. Preparation of ordered mesoporous Ag/WO₃ and its highly efficient degradation of acetaldehyde under visible-light irradiation. *J. Hazard. Mater.* **2010**, *178*, 427–433. [[CrossRef](#)]
9. Tahir, M.B.; Nabi, G.; Rafique, M.; Khalid, N.R. Nanostructured-based WO₃ photocatalysts: Recent development, activity enhancement, perspectives and applications for wastewater treatment. *Int. J. Environ. Sci. Technol.* **2017**, *14*, 2519–2542. [[CrossRef](#)]
10. Zhao, Z.G.; Miyauchi, M. Nanoporous-walled tungsten oxide nanotubes as highly active visible-light-driven photocatalysts. *Angew. Chem. Int. Ed.* **2008**, *47*, 7051–7055. [[CrossRef](#)]
11. Takeuchi, M.; Shimizu, Y.; Yamagawa, H.; Nakamuro, T.; Anpo, M. Preparation of the visible light responsive N³⁻-doped WO₃ photocatalyst by a thermal decomposition of ammonium paratungstate. *Appl. Catal. B* **2011**, *110*, 1–5. [[CrossRef](#)]
12. Adhikari, R.; Gyawali, G.; Sekino, T.; Wahn Lee, S. Microwave assisted hydrothermal synthesis of Ag/AgCl/WO₃ photocatalyst and its photocatalytic activity under simulated solar light. *J. Solid State Chem.* **2013**, *197*, 560–565. [[CrossRef](#)]
13. Poudel, M.B.; Lohani, P.C.; Kim, A.A. Synthesis of silver nanoparticles decorated tungsten oxide nanorods as high-performance supercapacitor electrode. *Chem. Phys. Lett.* **2022**, *804*, 139884. [[CrossRef](#)]
14. Theerthagiri, J.; Senthil, R.A.; Malathi, A.; Selvi, A.; Madhavan, J.; Ashokkumar, M. Synthesis and characterization of a CuS–WO₃ composite photocatalyst for enhanced visible light photocatalytic activity. *RSC Adv.* **2015**, *5*, 52718–52725. [[CrossRef](#)]
15. Poudel, M.B.; Awasthi, G.P.; Kim, H.J. Novel insight into the adsorption of Cr(VI) and Pb(II) ions by MOF derived Co–Al layered double hydroxide @hematite nanorods on 3D porous carbon nanofiber network. *Chem. Eng. J.* **2021**, *417*, 129312. [[CrossRef](#)]
16. Abe, R.; Takami, H.; Murakami, N.; Ohtani, B. Pristine simple oxides as visible light driven photocatalysts: Highly efficient decomposition of organic compounds over platinum-loaded tungsten oxide. *J. Am. Chem. Soc.* **2008**, *130*, 7780–7781. [[CrossRef](#)]
17. Dong, P.; Xu, N.; Xu, Y.; Wang, X. A study of Pt/WO₃-carrier catalysts for photocatalytic purification of NO gas. *Catal. Commun.* **2016**, *84*, 142–146. [[CrossRef](#)]
18. Dong, P.; Yang, B.; Liu, C.; Xu, F.; Xi, X.; Hou, G.; Shao, R. Highly enhanced photocatalytic activity of WO₃ thin films loaded with Pt–Ag bimetallic alloy nanoparticles. *RSC Adv.* **2017**, *7*, 947–956. [[CrossRef](#)]
19. Kim, Y.; Hong, J.W.; Lee, Y.W.; Kim, M.; Kim, D.; Yun, W.S.; Han, S.W. Synthesis of AuPt heteronanostructures with enhanced electrocatalytic activity toward oxygen reduction. *Angew. Chem. Int. Ed.* **2010**, *49*, 10197–10201. [[CrossRef](#)]
20. Zhao, S.; Yin, H.; Du, L.; Yin, G.; Tang, Z.; Liu, S. Three dimensional N-doped graphene/PtRu nanoparticle hybrids as high performance anode for direct methanol fuel cells. *J. Mater. Chem. A* **2014**, *2*, 3719–3724. [[CrossRef](#)]
21. Guo, S.; Dong, S.; Wang, E. Three-dimensional Pt-on-Pd bimetallic nanodendrites supported on graphene nanosheet: Facile synthesis and used as an advanced nanoelectrocatalyst for methanol oxidation. *ACS Nano* **2010**, *4*, 547–555. [[CrossRef](#)] [[PubMed](#)]
22. Yin, A.X.; Min, X.Q.; Zhu, W.; Wu, H.S.; Zhang, Y.W.; Yan, C.H. Multiply twinned Pt–Pd nanocicosahedrons as highly active electrocatalysts for methanol oxidation. *Chem. Commun.* **2012**, *48*, 543–545. [[CrossRef](#)] [[PubMed](#)]
23. Papadimitriou, S.; Armanyanov, S.; Valova, E.; Hubin, A.; Steenhaut, O.; Pavlidou, E.; Kokkinidis, G.; Sotiropoulos, S. Methanol oxidation at Pt–Cu, Pt–Ni, and Pt–Co electrode coatings prepared by a galvanic replacement process. *J. Phys. Chem. C* **2010**, *114*, 5217–5223. [[CrossRef](#)]
24. Xia, B.Y.; Wu, H.B.; Li, N.; Yan, Y.; Lou, X.W.; Wang, X. One-pot synthesis of Pt–Co alloy nanowire assemblies with tunable composition and enhanced electrocatalytic properties. *Angew. Chem. Int. Ed.* **2015**, *54*, 3797–3801. [[CrossRef](#)] [[PubMed](#)]
25. Yin, Z.; Zhou, W.; Gao, Y.; Ma, D.; Kiely, C.J.; Bao, X. Supported Pd–Cu bimetallic nanoparticles that have high activity for the electrochemical oxidation of methanol. *Chem. Eur. J.* **2012**, *18*, 4887–4893. [[CrossRef](#)] [[PubMed](#)]
26. Habibi, B.; Delnavaz, N. Carbon–ceramic supported bimetallic Pt–Ni nanoparticles as an electrocatalyst for oxidation of formic acid. *Int. J. Hydrogen Energy* **2011**, *36*, 9581–9590. [[CrossRef](#)]
27. Luo, J.Y.; Deng, S.Z.; Tao, Y.T.; Zhao, F.L.; Zhu, L.F.; Gong, L.; Chen, J.; Xu, N.S. Evidence of localized water molecules and their role in the gasochromic effect of WO₃ nanowire films. *J. Phys. Chem. C* **2009**, *113*, 15877–15881. [[CrossRef](#)]
28. Jian, L.Y.; Xue, X.C.; Wei, D.L.; Deng, W.Y.; Wei, L.; Hao, Y.W.; Lian, F.Z.; Qing, G.Z. Variable-temperature raman spectroscopic study of the hydrogen sensing mechanism in Pt–WO₃ nanowire film. *Appl. Phys. Lett.* **2013**, *102*, 113104. [[CrossRef](#)]

29. McBride, J.R.; Graham, G.W.; Peters, C.R.; Weber, W.H. Growth and characterization of reactively sputtered thin-film platinum oxides. *J. Appl. Phys.* **1991**, *69*, 1596–1604. [[CrossRef](#)]
30. Liang, M.-M.; Wang, Y.-H.; Shao, R.; Yang, W.-M.; Zhang, H.; Zhang, H.; Yang, Z.-L.; Li, J.-F.; Tian, Z.-Q. In situ electrochemical surface-enhanced Raman spectroscopy study of CO electrooxidation on PtFe nanocatalysts. *Electrochem. Commun.* **2017**, *81*, 38–42. [[CrossRef](#)]
31. Sugimura, F.; Sakai, N.; Nakamura, T.; Nakamura, M.; Ikeda, K.; Sakai, T.; Hoshi, N. In-situ observation of Pt oxides on the low index planes of Pt using surface enhanced raman spectroscopy. *Phys. Chem. Chem. Phys.* **2017**, *19*, 27570–27579. [[CrossRef](#)] [[PubMed](#)]
32. Huang, Y.F.; Kooyman, P.J.; Koper, M.T. Intermediate stages of electrochemical oxidation of single-crystalline platinum revealed by in situ Raman spectroscopy. *Nat. Commun.* **2016**, *7*, 12440. [[CrossRef](#)]
33. Li, L.; Xiao, S.; Li, R.; Cao, Y.; Chen, Y.; Li, Z.; Li, G.; Li, H. Nanotube array-like WO₃ photoanode with dual-layer oxygen-evolution cocatalysts for photoelectrocatalytic overall water splitting. *ACS Appl. Energy Mater.* **2018**, *1*, 6871–6880. [[CrossRef](#)]
34. Lei, F.; Li, Z.; Zhang, L.; Wang, Y.; Xu, S.; Lin, S. Facile synthesis of Pt–Cu (Ni, Co)/GNs–CD and their enhanced electro-catalytic activity for methanol oxidation. *J. Electrochem. Soc.* **2016**, *163*, F913–F918. [[CrossRef](#)]
35. Wang, H.; Wang, R.; Li, H.; Wang, Q.; Kang, J.; Lei, Z. Facile synthesis of carbon-supported pseudo-core@shell PdCu@Pt nanoparticles for direct methanol fuel cells. *Int. J. Hydrogen Energy* **2011**, *36*, 839–848. [[CrossRef](#)]
36. Han, C.; Lu, Y.; Zhang, J.; Ge, L.; Li, Y.; Chen, C.; Xin, Y.; Wu, L.; Fang, S. Novel PtCo alloy nanoparticle decorated 2D g-C₃N₄ nanosheets with enhanced photocatalytic activity for H₂ evolution under visible light irradiation. *J. Mater. Chem. A* **2015**, *3*, 23274–23282. [[CrossRef](#)]
37. Li, X.; Liu, Y.; Zhu, J.; Tsiakaras, P.; Shen, P.K. Enhanced oxygen reduction and methanol oxidation reaction over self-assembled Pt–M (M = Co, Ni) nanoflowers. *J. Colloid Interface Sci.* **2022**, *607*, 1411–1423. [[CrossRef](#)]
38. Qi, Y.; Yang, Z.; Jiang, Y.; Han, H.; Wu, T.; Wu, L.; Liu, J.; Wang, Z.; Wang, F. Platinum–copper bimetallic nanoparticles supported on TiO₂ as catalysts for photo-thermal catalytic toluene combustion. *ACS Appl. Nano Mater.* **2022**, *5*, 1845–1854. [[CrossRef](#)]
39. Peng, X.; Zhao, Y.; Chen, D.; Fan, Y.; Wang, X.; Wang, W.; Tian, J. One-pot synthesis of reduced graphene oxide supported PtCu_y catalysts with enhanced electro-catalytic activity for the methanol oxidation reaction. *Electrochim. Acta* **2014**, *136*, 292–300. [[CrossRef](#)]
40. Georgieva, J.; Valova, E.; Mintsouli, I.; Sotiropoulos, S.; Armanyanov, S.; Kakaroglou, A.; Hubin, A.; Steenhaut, O.; Dille, J. Carbon-supported Pt(Cu) electrocatalysts for methanol oxidation prepared by Cu electroless deposition and its galvanic replacement by Pt. *J. Appl. Electrochem.* **2013**, *44*, 215–224. [[CrossRef](#)]
41. Ghodbane, O.; Roué, L.; Bélanger, D. Study of the electroless deposition of Pd on Cu-modified graphite electrodes by metal exchange reaction. *Chem. Mater.* **2008**, *20*, 3495–3504. [[CrossRef](#)]
42. Khalakhan, I.; Vorokhta, M.; Xie, X.; Piliari, L.; Matolinová, I. On the interpretation of X-ray photoelectron spectra of Pt-Cu bimetallic alloys. *J. Electron Spectrosc. Relat. Phenom.* **2021**, *246*, 147027. [[CrossRef](#)]
43. Mathe, N.R.; Scriba, M.R.; Coville, N.J. Methanol oxidation reaction activity of microwave-irradiated and heat-treated Pt/Co and Pt/Ni nano-electrocatalysts. *Int. J. Hydrogen Energy* **2014**, *39*, 18871–18881. [[CrossRef](#)]
44. Biesinger, M.C.; Payne, B.P.; Grosvenor, A.P.; Lau, L.W.M.; Gerson, A.R.; Smart, R.S.C. Resolving surface chemical states in XPS analysis of first row transition metals, oxides and hydroxides: Cr, Mn, Fe, Co and Ni. *Appl. Surf. Sci.* **2011**, *257*, 2717–2730. [[CrossRef](#)]
45. Park, K.W.; Choi, J.H.; Kwon, B.K.; Lee, S.A.; Sung, Y.E. Chemical and electronic effects of Ni in Pt/Ni and Pt/Ru/Ni alloy nanoparticles in methanol electrooxidation. *J. Phys. Chem. B* **2002**, *106*, 1869–1877. [[CrossRef](#)]
46. Grosvenor, A.P.; Biesinger, M.C.; Smart, R.S.C.; McIntyre, N.S. New interpretations of XPS spectra of nickel metal and oxides. *Surf. Sci.* **2006**, *600*, 1771–1779. [[CrossRef](#)]
47. Desseigne, M.; Dirany, N.; Chevallier, V.; Arab, M. Shape dependence of photosensitive properties of WO₃ oxide for photocatalysis under solar light irradiation. *Appl. Surf. Sci.* **2019**, *483*, 313–323. [[CrossRef](#)]
48. Miyauchi, M. Photocatalysis and photoinduced hydrophilicity of WO₃ thin films with underlying Pt nanoparticles. *Phys. Chem. Chem. Phys.* **2008**, *10*, 6258–6265. [[CrossRef](#)]
49. Shiraishi, Y.; Sugano, Y.; Tanaka, S.; Hirai, T. One-pot synthesis of benzimidazoles by simultaneous photocatalytic and catalytic reactions on Pt@TiO₂ nanoparticles. *Angew. Chem. Int. Ed.* **2010**, *49*, 1656–1660. [[CrossRef](#)]
50. Shiraishi, Y.; Takeda, Y.; Sugano, Y.; Ichikawa, S.; Tanaka, S.; Hirai, T. Highly efficient photocatalytic dehalogenation of organic halides on TiO₂ loaded with bimetallic Pd–Pt alloy nanoparticles. *Chem. Commun.* **2011**, *47*, 7863–7865. [[CrossRef](#)]
51. Gulen, M.; Yildirim, G.; Bal, S.; Varilci, A.; Belenli, I.; Oz, M. Role of annealing temperature on microstructural and electro-optical properties of ITO films produced by sputtering. *J. Mater. Sci. Mater. Electron.* **2012**, *24*, 467–474. [[CrossRef](#)]
52. Kotlyar, K.P.; Kudryashov, D.A.; Soshnikov, I.P.; Uvarov, A.V.; Reznik, R.R. Temperature annealing effect on ITO film. *J. Phys. Conf. Ser.* **2018**, *1124*, 041035. [[CrossRef](#)]
53. Wang, X.H.; Li, J.G.; Kamiyama, H.; Moriyoshi, Y.; Ishigaki, T. Wavelength-sensitive photocatalytic degradation of methyl orange in aqueous suspension over Iron(III)-doped TiO₂ nanopowders under UV and visible light irradiation. *J. Phys. Chem. B* **2006**, *110*, 6804–6809. [[CrossRef](#)] [[PubMed](#)]
54. Haleem, A.; Shafiq, A.; Chen, S.Q.; Nazar, M. A comprehensive review on adsorption, photocatalytic and chemical degradation of dyes and nitro-compounds over different kinds of porous and composite materials. *Molecules* **2023**, *28*, 1081. [[CrossRef](#)]

55. Begum, R.; Najeeb, J.; Sattar, A.; Naseem, K.; Irfan, A.; Al-Sehemi, A.G.; Farooqi, Z.H. Chemical reduction of methylene blue in the presence of nanocatalysts: A critical review. *Rev. Chem. Eng.* **2020**, *36*, 749–770. [[CrossRef](#)]
56. Dong, P.; Wang, Y.; Li, H.; Li, H.; Ma, X.; Han, L. Shape-controllable synthesis and morphology-dependent photocatalytic properties of Ag₃PO₄ crystals. *J. Mater. Chem. A* **2013**, *1*, 6955–6963. [[CrossRef](#)]
57. Chen, C.; Wang, Q.; Lei, P.; Song, W.; Ma, W.; Zhao, J. Photodegradation of dye pollutants catalyzed by porous K₃PW₁₂O₄₀ under visible Irradiation. *Environ. Sci. Technol.* **2006**, *40*, 3965–3970. [[CrossRef](#)]
58. Pan, C.; Zhu, Y. New type of BiPO₄ oxy-acid salt photocatalyst with high photocatalytic activity on degradation of dye. *Environ. Sci. Technol.* **2010**, *44*, 5570–5574. [[CrossRef](#)]
59. Lee, H.; Choi, W. Photocatalytic oxidation of arsenite in TiO₂ suspension: kinetics and mechanisms. *Environ. Sci. Technol.* **2002**, *36*, 3872–3878. [[CrossRef](#)]
60. Poudel, M.B.; Kim, A.A.; Lohani, P.C.; Yoo, D.J.; Kim, H.J. Assembling zinc cobalt hydroxide/ternary sulfides heterostructure and iron oxide nanorods on three-dimensional hollow porous carbon nanofiber as high energy density hybrid supercapacitor. *J. Energy Storage* **2023**, *60*, 106713. [[CrossRef](#)]
61. Klahr, B.; Gimenez, S.; Fabregat-Santiago, F.; Bisquert, J.; Hamann, T.W. Photoelectrochemical and impedance spectroscopic investigation of water oxidation with “Co–Pi”-coated hematite electrodes. *J. Am. Chem. Soc.* **2012**, *134*, 16693–16700. [[CrossRef](#)] [[PubMed](#)]
62. Vida, G.; Josepovits, V.K.; Gyor, M.; Deak, P. Characterization of tungsten surfaces by simultaneous work function and secondary electron emission measurements. *Microsc. Microanal.* **2003**, *9*, 337–342. [[CrossRef](#)] [[PubMed](#)]
63. Yella, A.; Gautam, U.K.; Mugnaioli, E.; Panthöfer, M.; Bando, Y.; Golberg, D.; Kolb, U.; Tremel, W. Asymmetric tungsten oxide nanobrushes via oriented attachment and ostwald ripening. *CrystEngComm* **2011**, *13*, 4074–4081. [[CrossRef](#)]
64. Eastman, D.E. Photoelectric work functions of transition, rare-earth, and noble metals. *Phys. Rev. B* **1970**, *2*, 1–2. [[CrossRef](#)]
65. Michaelson, H.B. The work function of the elements and its periodicity. *J. Appl. Phys.* **1977**, *48*, 4729–4733. [[CrossRef](#)]
66. Ishii, R.; Matsumura, K.; Sakai, A.; Sakata, T. Work function of binary alloys. *Appl. Surf. Sci.* **2001**, *169*, 658–661. [[CrossRef](#)]
67. Tsukamoto, D.; Shiro, A.; Shiraishi, Y.; Sugano, Y.; Ichikawa, S.; Tanaka, S.; Hirai, T. Photocatalytic H₂O₂ production from ethanol/O₂ system using TiO₂ loaded with Au–Ag bimetallic alloy nanoparticles. *ACS Catal.* **2012**, *2*, 599–603. [[CrossRef](#)]
68. Arai, T.; Yanagida, M.; Konishi, Y.; Iwasaki, Y.; Sugihara, H.; Sayama, K. Efficient complete oxidation of acetaldehyde into CO₂ over CuBi₂O₄/WO₃ composite photocatalyst under visible and UV light irradiation. *J. Phys. Chem. C* **2007**, *111*, 7574–7577. [[CrossRef](#)]
69. Weng, B.; Wu, J.; Zhang, N.; Xu, Y.J. Observing the role of graphene in boosting the two-electron reduction of oxygen in graphene–WO₃ nanorod photocatalysts. *Langmuir* **2014**, *30*, 5574–5584. [[CrossRef](#)]
70. D’Arienzo, M.; Armelao, L.; Mari, C.M.; Polizzi, S.; Ruffo, R.; Scotti, R.; Morazzoni, F. Macroporous WO₃ thin films active in NH₃ sensing: Role of the hosted Cr isolated centers and Pt nanoclusters. *J. Am. Chem. Soc.* **2011**, *133*, 5296–5304. [[CrossRef](#)]
71. Rick, C.; Schroden, M.A.-D.; Blanford, F.C.; Stein, A. Optical properties of inverse opal photonic crystals. *Chem. Mater.* **2002**, *14*, 3305–3315.
72. Liu, C.; Lü, H.; Yu, C.; Ding, B.; Ye, R.; Ji, Y.; Dai, B.; Liu, W. Novel FeWO₄/WO₃ nanoplate with p–n heterostructure and its enhanced mechanism for organic pollutants removal under visible-light illumination. *J. Environ. Chem. Eng.* **2020**, *8*, 104044. [[CrossRef](#)]
73. Ibrahim, Y.O.; Gondal, M.A.; Alaswad, A.; Moqbel, R.A.; Hassan, M.; Cevik, E.; Qahtan, T.F.; Dastageer, M.A.; Bozkurt, A. Laser-induced anchoring of WO₃ nanoparticles on reduced graphene oxide sheets for photocatalytic water decontamination and energy storage. *Ceram. Int.* **2020**, *46*, 444–451. [[CrossRef](#)]
74. Liu, Y.; Li, M.; Zhang, Q.; Qin, P.; Wang, X.; He, G.; Li, L. One-step synthesis of a WO₃-CuS nanosheet heterojunction with enhanced photocatalytic performance for methylene blue degradation and Cr(VI) reduction. *J. Chem. Technol. Biotechnol.* **2019**, *95*, 665–674. [[CrossRef](#)]
75. Sharma, S.; Basu, S. Highly reusable visible light active hierarchical porous WO₃/SiO₂ monolith in centimeter length scale for enhanced photocatalytic degradation of toxic pollutants. *Sep. Purif. Technol.* **2020**, *231*, 115916. [[CrossRef](#)]
76. Singh, J.; Arora, A.; Basu, S. Synthesis of coral like WO₃/g-C₃N₄ nanocomposites for the removal of hazardous dyes under visible light. *J. Alloys Compd.* **2019**, *808*, 151734. [[CrossRef](#)]
77. Zhang, J.; Fu, X.; Hao, H.; Gan, W. Facile synthesis 3D flower-like Ag@WO₃ nanostructures and applications in solar-light photocatalysis. *J. Alloys Compd.* **2018**, *757*, 134–141. [[CrossRef](#)]
78. Xie, R.; Fang, K.; Liu, Y.; Chen, W.; Fan, J.; Wang, X.; Ren, Y.; Song, Y. Z-scheme In₂O₃/WO₃ heterogeneous photocatalysts with enhanced visible-light-driven photocatalytic activity toward degradation of organic dyes. *J. Mater. Sci.* **2020**, *55*, 11919–11937. [[CrossRef](#)]
79. Prabhu, S.; Cindrella, L.; Kwon, O.J.; Mohanraju, K. Photoelectrochemical and photocatalytic activity of TiO₂-WO₃ heterostructures boosted by mutual interaction. *Mater. Sci. Semicond. Process.* **2018**, *88*, 10–19. [[CrossRef](#)]

Disclaimer/Publisher’s Note: The statements, opinions and data contained in all publications are solely those of the individual author(s) and contributor(s) and not of MDPI and/or the editor(s). MDPI and/or the editor(s) disclaim responsibility for any injury to people or property resulting from any ideas, methods, instructions or products referred to in the content.